Iterated upwind schemes for gas dynamics

Piotr K. Smolarkiewicz [a,*], Joanna Szmelter [b]

[a] *National Center for Atmospheric Research, P.O. Box 3000, Boulder, CO 80307, USA*
[b] *Loughborough University, Wolfson School of Mechanical and Manufacturing Engineering, Loughborough, Leicestershire LE11 3TU, UK*

ARTICLE INFO

ABSTRACT

A class of high-resolution schemes established in integration of anelastic equations is extended to fully compressible flows, and documented for unsteady (and steady) problems through a span of Mach numbers from zero to supersonic. The schemes stem from iterated upwind technology of the multidimensional positive definite advection transport algorithm (MPDATA). The derived algorithms employ standard and modified forms of the equations of gas dynamics for conservation of mass, momentum and either total or internal energy as well as potential temperature. Numerical examples from elementary wave propagation, through computational aerodynamics benchmarks, to atmospheric small- and large-amplitude acoustics with intricate wave-flow interactions verify the approach for both structured and unstructured meshes, and demonstrate its flexibility and robustness.

© 2008 Elsevier Inc. All rights reserved.

1. Introduction

There is a continuing quest for general (template) algorithms capable of solving incompressible and compressible fluid equations throughout a range of flow regimes, multiplicity of scales and the variety of applications; e.g. [1–3]. One obvious motivation is the cost effectiveness resulting from reduced maintenance of unified, large multi-purpose codes in research and practice; another is an increasingly growing interest in multiscale multiphysics applications crossing boundaries of traditional disciplinary areas. A particular class of such versatile solvers was developed for simulation of atmospheric flows. These solvers are built around the high-resolution upwind method MPDATA broadly documented in the literature; see [4,5] for reviews. Upwind and high-resolution methods have a long history in simulation of compressible flows; see [6] for a succinct review. Even though MPDATA dates back to the early eighties [7,8], and MPDATA-based fluid solvers to the early nineties [9,10], the approach was primarily used to solve soundproof (incompressible and anelastic) equations of geophysical fluid dynamics on structured grids [4,11]. However, MPDATA solvers should be adaptable to multiphysics applications and a wide range of flow speeds. Yet apart from [12–14], where we merely expose the potential of the approach, their applicability to gas dynamics is largely unknown. Here, we complement the earlier work with a study of a family of algorithms for a range of compressible flows, and report our findings on their performance in applications from transient to a steady-state limit, in calculations representative of elementary acoustics, aerodynamics, and atmospheric flows. To address such diverse applications, we develop solvers, employing standard and modified forms of the equations of gas dynamics for conservation of mass, momentum and either total or internal energy as well as potential temperature. While conserving total energy is standard in engineering applications, conserving potential temperature or internal energy may benefit atmospheric applications with ambient temperature/density stratification [15,16].

---

* Corresponding author. Tel.: +1 303 497 8972; fax: +1 303 497 8181.
E-mail addresses: smolar@ucar.edu (P.K. Smolarkiewicz), j.szmelter@lboro.ac.uk (J. Szmelter).

Placed among high-resolution methods, the MPDATA solvers evince some distinct features [17] desirable in simulation of compressible flows. Perhaps the most important are the genuine multidimensionality of MPDATA [8], underlying formulation in curvilinear coordinates [18,10], and easy accuracy-sustaining generalizations to unstructured meshes [19,12,13]. In contrast to many other nonoscillatory methods, the basic MPDATA is formally second-order accurate in arbitrary dimensional flows, but only sign preserving rather than monotone. While sign preservation ensures nonlinear stability and together with second-order accuracy suffices in many applications, monotonicity preservation and enhanced accuracy are available as options [20,21]. Because of the geophysical heritage, MPDATA solvers were designed to facilitate simulation of turbulent motions with implicit representations of continuous spectra of dispersive waves. In consequence, the resulting algorithms for governing conservation laws favor a Newtonian form of the governing PDEs (with accelerations and forces appearing on the left- and right-hand-side, respectively) rather than the standard form used in simulation of gas dynamics (with forces combined with advective fluxes under the divergence operator on the rhs). Although equivalent, the two formulations inspire different approximation techniques and accumulate different pools of experience. Consequently, exploiting these distinct features of MPDATA may open alternative avenues, perhaps as much for engineering applications as for simulation of atmospheric acoustics and compressible flow responses to localized large-amplitude perturbations (such as volcano eruption; hereafter, "extreme events" for brevity).

In the following section we summarize the notion of the MPDATA-based methods for fluids. Section 3 presents salient details of the analytical and numerical aspects of the algorithms customized for compressible flows. Section 4 reports on a range of benchmark calculations and explores relative merits of the schemes. With bolstered confidence in the integrity and robustness of the approach, in Section 5, we simulate small- and large-amplitude acoustic wave propagation in complex anisotropic and inhomogeneous media with intricate wave dynamics. This simulation demonstrates the generality of our approach, as it depends on combining the capabilities of anelastic and compressible solvers. Remarks in Section 6 conclude the paper.

2. Notion of MPDATA flow solvers

2.1. Homogeneous advection equation

Consider first the elementary advection equation

$$\frac{\partial \phi}{\partial t} = -\nabla \cdot (\mathbf{V}\phi), \tag{1}$$

where $\phi = \phi(\mathbf{x}, t)$ is a scalar field transported with an arbitrary flow $\mathbf{V} = \mathbf{V}(\mathbf{x}, t)$. Integrating (1) in time and over the volume of a cell surrounding vertex i results in

$$\phi_i^{n+1} = \phi_i^n - \frac{\delta t}{\mathscr{V}_i} \sum_{j=1}^{l(i)} F_j^{\perp} S_j. \tag{2}$$

Here the summation is over edges connecting vertex i with one of its immediate neighbors j. There are $l(i)$ edges connecting the vertex i with its neighbors, and S_j refers both to the cell face pierced by the jth edge and its surface area; see [12] for graphic illustrations. Eq. (2) is exact, given ϕ_i^{n+1} and ϕ_i^n are interpreted as the mean values of ϕ within the volume $\mathscr{V}_i$ of the cell containing vertex i; while $F_j^{\perp}$ is interpreted as the mean normal flux through the cell face S_j averaged over temporal increment δt. The approximation amounts to specifying fluxes $F_j^{\perp}$ in terms of data available on the mesh. In MPDATA, all fluxes assume the upwind (alias donor cell) functional form

$$F_j^{\perp}\left(\phi_i, \phi_j, V_j^{\perp}\right) = \left[V_j^{\perp}\right]^+ \phi_i + \left[V_j^{\perp}\right]^- \phi_j, \tag{3}$$

where

$$[V]^+ \equiv 0.5(V + |V|), \quad [V]^- \equiv 0.5(V - |V|), \tag{4}$$

and normal velocity $V^{\perp}$ is evaluated at the face S_j. The nonnegative/nonpositive parts of $V_j^{\perp}$ always coincide with outflow/inflow from the ith cell.

In its essence, MPDATA is constructed using properties of iterated upwinding. It consists of a series of the first-order upwind steps: the first step provides a first-order-accurate solution, and subsequent steps compensate the truncation errors of the preceding steps, derived analytically from a modified equation analysis [22] of the upwind scheme. This leads to a compact functional form of MPDATA:

$$\phi_i^{(k)} = \phi_i^{(k-1)} - \frac{\delta t}{\mathscr{V}_i} \sum_{j=1}^{l(i)} F_j^{\perp}\left(\phi_i^{(k-1)}, \phi_j^{(k-1)}, V_j^{\perp,(k)}\right) S_j, \tag{5}$$

with $k = 1, \ldots, IORD$ such that

$$\phi^{(0)} \equiv \phi^n; \ \phi^{(IORD)} \equiv \phi^{n+1}$$

$$V^{\perp,(k+1)} = V^{\perp}\left(\mathbf{V}^{(k)}, \phi^{(k)}, \nabla\phi^{(k)}\right); \ V_j^{\perp,(1)} \equiv V^{\perp}|_j^{n+1/2}.$$

In (5), the first iteration uses for arguments of $F_j^\perp$ the transported field values from the preceding time step and an $\mathcal{O}(\delta t^2)$ estimate of the velocity at $t^{n+1/2}$. Deriving the explicit form of compensating velocity $V^{\perp,(k+1)}$, used in subsequent iterations, requires assessing the leading truncation error of upwind differencing specified in (2)–(4). A standard approach is to expand all discrete data into a Taylor series in time and space about a common point $(\mathbf{x}, t)$, and then to represent higher-order temporal derivatives in terms of spatial derivatives. For example, the expansion about the intermediate time $t^{n+1/2}$ and point s_j where the edge pierces the face [12] allows to decompose the upwind flux in (3) into a time-centered flux through the face and the first-order truncation error flux of a predominantly diffusive character

$$F_j^\perp = \{V^\perp \phi + Error\}|_{s_j}^{n+1/2}, \tag{6}$$

with *Error* dominated by $\mathcal{O}(\delta r, \delta t)$ terms proportional to components of $-\nabla\phi$; here δr refers to the characteristic linear size of the control volume. Noting that the form of the error is an attribute of the functional form of upwind differencing — i.e., it remains the same for all k in (5) — and writing the error as the advective flux of ϕ, defines the compensating velocity in (5) as $V^{\perp,(k+1)} \equiv -(Error/\phi)^{(k)}$. In particular,

$$V^\perp\Big|_{s_j}^{(k+1)} = \left\{ 0.5\,|V^\perp|\left(\frac{1}{|\phi|}\frac{\partial|\phi|}{\partial r}\right)(r_j - r_i) - 0.5\,V^\perp\left(\frac{1}{|\phi|}\frac{\partial|\phi|}{\partial r}\right)(r_i - 2r_{s_j} + r_j) - 0.5\delta t V^\perp\left(\mathbf{V}\cdot\frac{1}{|\phi|}\nabla|\phi|\right) - 0.5\delta t V^\perp(\nabla\cdot\mathbf{V}) \right\}\Big|_{s_j}^{(k)}, \tag{7}$$

where, $r(\lambda) = r_i + \lambda(r_j - r_i); \lambda \in [0, 1]$. The entire process of estimating the residual error and compensating it can be continued, iteration after iteration, reducing the magnitude of the truncation error while preserving the sign of transported variables. In practice, one corrective iteration suffices for recovering the second-order accuracy of time-space centered schemes.

The analytic expression for basic MPDATA algorithm in (5) and (7) applies to an arbitrary mesh, either structured or unstructured. The details of representing differential operators in (7) depend on the adopted data structure. Typically they employ centered differencing commensurate with the mesh. In this paper we employ MPDATA for various meshes and grids. For details of specific implementations the interested reader is referred to earlier works [8,18,12], and for the guidance to options (such as monotonicity preservation or higher-order accuracy) extending MPDATA beyond the basic scheme to the reviews in [4,5].

2.2. Fluid solvers

Derivation of the MPDATA-based schemes for fluids starts with the truncation error analysis of two-time-level approximations for an archetype inhomogeneous PDE for advection-dominated flows, e.g.

$$\frac{\partial\phi}{\partial t} + \nabla\cdot(\mathbf{V}\phi) = R, \tag{8}$$

in abstraction from any particular assumptions on the nature of physical forcing R and its relation to densities ϕ of dependent variables, but driven solely by the requirement of the second-order accuracy for arbitrary smooth $\phi(\mathbf{x}, t)$ and transporting velocity $\mathbf{V}(\mathbf{x}, t)$. Assuming availability of a two-time-level nonoscillatory advection scheme that is fully second-order-accurate for the homogeneous counterpart of (8) (viz. MPDATA), one can design a family of model algorithms with different degrees of the overall accuracy and complexity [9,10]. Hereafter, for brevity and consistency with nomenclature introduced in [23], we shall refer to such solvers as NFT, for "nonoscillatory forward-in-time".

Extending the truncation error analysis of the homogeneous problem (1) to (8) modifies (6) with the $\mathcal{O}(\delta t)$ advective flux of R on the rhs; i.e.,

$$F_j^\perp = \{V^\perp \phi + Error_{adv} - 0.5\delta t V^\perp R\}|_{s_j}^{n+1/2}, \tag{9}$$

where $Error_{adv}$ refers to the error of upwind differencing in (2)–(4). The forcing-related error can be compensated in various ways [9,10,4]. One, particularly useful for applications, variant of the NFT integral for (8) takes a simple form

$$\phi_i^{n+1} = \mathscr{A}_i(\phi^n + 0.5\delta t R^n, \mathbf{V}^{n+1/2}) + 0.5\delta t R_i^{n+1}, \tag{10}$$

where the transport operator $\mathscr{A}$ symbolizes the NFT advection scheme such as MPDATA — e.g. the scheme in (5) — and a control volume mean R^{n+1} either depends implicitly on problem variables or is an explicit second-order estimate. For second-order convergence it would suffice to provide only an $\mathcal{O}(\delta t)^2$ estimate, yet with $R^{n+1} = R(t + \delta t) + \mathcal{O}(\delta t^3)$ the algorithm (10) admits explicit schemes for wave propagation with zero amplitude error; see appendix B in [10].

Although (10) may appear as a form of Strang splitting [24], it is indeed an unsplit algorithm that approximates the space-time control volume integral of (8) as

$$\phi_i^{n+1} = \phi_i^n - \frac{\delta t}{\mathscr{V}_i}\sum_{j=1}^{l(i)}\{V^\perp\phi\}|_{s_j}^{n+1/2}S_j + 0.5\delta t\left(R_i^n + R_i^{n+1}\right) + \delta t\mathcal{O}(\delta t^2, \delta t\delta r, \delta r^2). \tag{11}$$

Furthermore, (10) has an illuminating geometric interpretation in a spacetime continuum. Namely, it is congruent with a trajectory integral of the Lagrangian counterpart of (8)

$$\frac{D\mathscr{J}\phi}{Dt} = \mathscr{J}R,$$ (12)

evaluated to the second-order accuracy with the trapezoidal rule

$$\phi_i^{n+1} = \widehat{\mathscr{J}}_i\phi_o + 0.5\delta t(\widehat{\mathscr{J}}_i R_o + R_i^{n+1}) = \widehat{\mathscr{J}}_i(\phi + 0.5\delta t R)_o + 0.5\delta t R_i^{n+1},$$ (13)

along the flow trajectory $\dot{\mathbf{x}} = \mathbf{V}$ connecting mesh-point $(\mathbf{x}_i, t^{n+1})$ with the foot $(\mathbf{x}_o(\mathbf{x}_i, t^{n+1}), t^n)$; the subscript "o" denotes mapping to the foot, akin to advection [25,26]. Recall that the flow Jacobian $\mathscr{J} \equiv \det(\partial\mathbf{x}/\partial\mathbf{x}_o)$ satisfies the Euler expansion formula $D/Dt \ln \mathscr{J} = \nabla \cdot \mathbf{V}$ [27], whereupon the solution of (12) for ϕ representing the mass density ρ is simply $\rho_i^{n+1} = \rho_o \widehat{\mathscr{J}}_i$, with the inverse flow Jacobian $\widehat{\mathscr{J}} \equiv \det(\partial\mathbf{x}_o/\partial\mathbf{x})$; note that both $\mathscr{J}$ and $\widehat{\mathscr{J}}$ equal unity at the foot. Inspecting (10) versus (13) reveals that the two schemes are equivalent to $\mathcal{O}(\delta t^3)$ as $\delta r \to 0$. Here, we mention this congruency only to strengthen some heuristic arguments and to aid the interpretation of finite-volume solvers (10) used later in this paper. In practice, however, the congruency of (10) and (13) facilitates the design of unified Eulerian/semi-Lagrangian fluids models [28,29], and so is useful beyond fostering the interpretation of complicated fluid schemes.

There are two elements defining the solver in (10): (i) the choice of the transport operator $\mathscr{A}$; and (ii) the approach for evaluating R^{n+1} at the rhs. In principle, any two-time-level advection algorithm can be used for $\mathscr{A}$ that is nonlinearly stable (e.g. nonoscillatory) and at least second-order-accurate for an arbitrary time-independent flow. However, our numerical experience with advanced fluid models does not extend beyond MPDATA and its derivatives. Notably, among nonoscillatory schemes MPDATA appears to have unique dissipative properties [17] in mimicking the action of explicit subgrid-scale turbulence models where flow is underresolved – cf. [30–33] and references therein. This makes MPDATA methods suitable for direct numerical simulation (DNS) and large-eddy simulation (LES) as well as for implicit LES (ILES) [11]. This dissipative property of MPDATA plays an important role in handling discontinuities not accounted for in the derivation of (10). Formally, (10) only provides a means of suppressing numerical oscillations but does not ensure perfectly oscillation free solutions. If the latter is required, additional enhancement can be employed [34,35,13]. The evaluation of R^{n+1} in (10) depends on the adopted form of the governing PDEs and selection of dependent variables. The standard formulations of hyperbolic conservation laws via mass, momentum and energy, require iterative determination of the rhs, yet remain efficient because the transport term $\mathscr{A}_i$ in (10) is evaluated only once per time step. In the next section, we present several solver designs to show the flexibility of the approach. We support theoretical considerations with numerical examples using both structured and unstructured meshes, to illustrate that the concept of the NFT methods does not depend on spatial discretization.

3. Compressible flow solvers

3.1. Analytic formulation

From the perspective of the archetype Eq. (8), the mass continuity equation

$$\frac{\partial\rho}{\partial t} + \nabla \cdot (\mathbf{V}\rho) = 0$$ (14)

is distinct among the governing PDEs of ideal gas dynamics, because it is homogeneous for all flows. The conservation of momenta $q^I \equiv \rho V^I$ (for $I = 1, 2, 3$) adheres to the form (8) with the pressure-gradient force on the rhs

$$\frac{\partial q^I}{\partial t} + \nabla \cdot (\mathbf{V}q^I) = -\frac{\partial p}{\partial x^I}.$$ (15)

Assuming (for simplicity of the presentation) adiabatic processes, laws accounting for conservation of thermodynamic properties of the fluid can be written alternatively in terms of the internal energy $e = \rho c_v T$ – where T and c_v denote, standardly, the temperature and specific heat at constant volume – or the total energy $E = e + (1/2)\rho\mathbf{V}^2$, respectively, as

$$\frac{\partial e}{\partial t} + \nabla \cdot (\mathbf{V}e) = -p\nabla \cdot \mathbf{V}$$ (16)

or

$$\frac{\partial E}{\partial t} + \nabla \cdot (\mathbf{V}E) = -\nabla \cdot (\mathbf{V}p).$$ (17)

The latter equation can be written in a modified form

$$\frac{\partial E}{\partial t} + \nabla \cdot (\widetilde{\mathbf{V}}E) = 0; \quad \widetilde{\mathbf{V}} \equiv \mathbf{V}(1 + p/E),$$ (18)

that although mathematically equivalent to (17), motivates alternate realizations of the template algorithm (10).

Yet another form – important for simulating low Mach number flows of compressible stratified fluids, such as planetary atmospheres – employs an invariant of adiabatic processes $\theta \equiv T(p/p_0)^{-R/c_p}$, referred to as the potential temperature in the meteorological literature.[1] Here R and c_p are the specific gas constant and heat at constant pressure, respectively, and the constant p_0 denotes a reference pressure. Defining $\Theta \equiv \rho\theta$, the alternative thermodynamic conservation law takes a simple form

$$\frac{\partial \Theta}{\partial t} + \nabla \cdot (\mathbf{V}\Theta) = 0. \tag{19}$$

3.2. Numerical approximations

In order to emphasize numerical commonalities of the considered sets of the governing PDEs – consisting of (14) and (15), together with either (16)–(18) or (19) – it is convenient to denote the respective vectors of dependent variables $[\rho, \mathbf{q}, e]$, $[\rho, \mathbf{q}, E]$ or $[\rho, \mathbf{q}, \Theta]$ compactly as $\boldsymbol{\Phi}$; here $\mathbf{q} \equiv [q^1, q^2, q^3]$. Consistently, the respective vectors of the associated right-hand-sides $[0, -\nabla p, -p\nabla \cdot \mathbf{V}]$, $[0, -\nabla p, -\nabla \cdot (\mathbf{V}p)]$, or $[0, -\nabla p, 0]$ are denoted as $\mathbf{R}$. With this notation, the scalar archetype inhomogeneous PDE (8) and the template algorithm (10) can be extended to any of the considered sets of PDEs, respectively, as

$$\frac{\partial \boldsymbol{\Phi}}{\partial t} + \nabla \cdot (\mathbf{V}\boldsymbol{\Phi}) = \mathbf{R}, \tag{20}$$

and

$$\forall_i \quad \boldsymbol{\Phi}_i^{n+1} = \boldsymbol{\Phi}_i^* + 0.5\delta t \mathbf{R}_i^{n+1}. \tag{21}$$

In (21), $\boldsymbol{\Phi}^* \equiv \mathscr{A}(\boldsymbol{\Phi}^n + 0.5\delta t \mathbf{R}^n, \widehat{\mathbf{V}}^{n+1/2})$ is a shorthand for the first term on the rhs of (10) evaluated independently for each component of $\boldsymbol{\Phi}$, and $\widehat{\mathbf{V}} \equiv \mathbf{V}$ in all cases except for the integral of the modified total energy Eq. (18) where $\widehat{\mathbf{V}} \equiv \breve{\mathbf{V}}$.

Given the availability of a suitable transport operator $\mathscr{A}$, implementing the template (21) requires two specifications: (i) a first-order estimate of the advecting velocity $\widehat{\mathbf{V}}$ at $t^{n+1/2}$; and (ii) a second-order estimate of the rhs $\mathbf{R}$ at t^{n+1}. For $\widehat{\mathbf{V}}^{n+1/2}$ one can use either a linear extrapolation, or a first-order solution to the governing system [10]. Here, we use exclusively the linear extrapolation $\widehat{\mathbf{V}}^{n+1/2} = (1 + \beta)\widehat{\mathbf{V}}^n - \beta\widehat{\mathbf{V}}^{n-1}$, with $\beta = 0.5(t^{n+1} - t^n)/(t^n - t^{n-1})$. A provision of an $\mathcal{O}(\delta t^3)$ estimate of R^{n+1} is the crux of the approach. Clearly, it depends on the specific problem and admits a number of options. The simplest example is a realization of (21) for isentropic thermodynamics (19): After solving two advection equations (14) and (19) for ρ and Θ, respectively, evaluating pressure-gradient forces for the rhs of the momentum-component equation (15) follows readily, by noting that the definition of θ and the ideal gas law $p = \rho RT$ imply $p \propto \Theta^\gamma$, with $\gamma \equiv c_p/c_v$; see [13] for a detailed discussion and the demonstration of the second-order convergence on an unstructured mesh.

In general, however, solving any form of the energy equations (16), (17), or (18) implies, effectively, an implicit problem due to the dependence of pressure on the energy and flow. To proceed in the spirit of the trapezoidal rule, we iterate (21) as

$$\forall_i \quad \boldsymbol{\Phi}_i^{n+1,\mu} = \boldsymbol{\Phi}_i^* + 0.5\delta t \mathbf{R}_i^{n+1,\mu-1}, \tag{22}$$

where $\mu = 1, \ldots, m$ numbers successive iterations, and the first guess $\mathbf{R}^{n+1,0}$ is either a first-order predictor or, simply, $\mathbf{R}^{n+1,0} = \mathbf{R}^n$. Importantly, the computationally-intensive explicit part $\boldsymbol{\Phi}_i^*$ is evaluated only once per time step – by executing the advection module prior to (22) – thus remaining fixed during the iteration process. Furthermore, although (22) is formally valid for the components of $\boldsymbol{\Phi}$ with identically vanishing associated rhs, in practice it is executed only for the components with nontrivial R.

Formally, the convergence of the iteration in (22) may be argued in terms of the mean value theorem for mappings (in Banach spaces); e.g. Theorem VII.5.2 in [37]. Normalizing (21) and (22),[2] then subtracting from (22) its limit (21), and assuming the differentiability of the mapping $\mathbf{R}(\boldsymbol{\Phi})$ ensures

$$\|\boldsymbol{\Phi}^{n+1,\mu} - \boldsymbol{\Phi}^{n+1}\| = 0.5\delta t\|\mathbf{R}(\boldsymbol{\Phi}^{n+1,\mu-1}) - \mathbf{R}(\boldsymbol{\Phi}^{n+1})\| \leqslant 0.5\delta t \sup\|\partial\mathbf{R}/\partial\boldsymbol{\Phi}\|\|\boldsymbol{\Phi}^{n+1,\mu-1} - \boldsymbol{\Phi}^{n+1}\|, \tag{23}$$

where the supremum is taken along the interval $\boldsymbol{\Phi}^{n+1,\mu-1} + \lambda\|\boldsymbol{\Phi}^{n+1,\mu-1} - \boldsymbol{\Phi}^{n+1}\|$, with $0 \leqslant \lambda \leqslant 1$. The assumed continuity of the derivative assures that there exist a sufficiently small δt, such that $0.5\delta t \sup\|\partial\mathbf{R}/\partial\boldsymbol{\Phi}\| < 1$, for which (22) converges. On the other hand, from linear-analysis arguments, the elements of the Jacobi matrix $\partial\mathbf{R}/\partial\boldsymbol{\Phi}$ represent reciprocals of the characteristic time-scales of (20); e.g. $c/\delta r$.[3] Consequently, using δt that satisfies the Courant–Friedrichs–Lewy (CFL) stability condition for a governing PDE system (20) should suffice for the iteration convergence. Indeed, our numerical experience confirms a rapid convergence of (22); e.g. the observed values of $(p^{n+1,\mu} - p^{n+1,\mu-1})$ decrease by one to two orders of magnitude per iteration,

---

[1] The potential temperature has been introduced by Helmholtz in 1888 as a convenient entropy function for studying atmospheric motions; $\theta = \exp(s/c_p)$ for ideal fluids, where s denotes specific entropy. Nonetheless, it has been also recognized that θ embodies a more general idea not necessarily tantamount with entropy; cf. [36] for an early discussion.

[2] Consider dividing (14) by ρ_o, (15) by $\rho_o c_o$, (16)–(18) by $\rho_o c_o^2$, and (19) by T_o; where the subscript $_o$ refers to free stream values, and c denotes the speed of sound.

[3] Consider a 1D isentropic flow linearized about the quiescent free stream, and assume a single Fourier mode solution with the wave-number $k = 1/\delta r$.

within the first few iterations. Moreover, even with $R^{n+1,0} = R^n$, $m = 2$ provides second-order-accurate solutions to (8), while $m = 3$ also ensures an $\mathcal{O}(\delta t^3)$ estimate of R^{n+1}.

The abstract framework of (22) admits sufficient flexibility to accommodate a variety of specific fluid equations and computer program designs. For example, its utility has been demonstrated for nonhydrostatic simulations of anelastic stratified flows on rotating spheres [38], of viscoelastic biomechanics [39], and more recently of magneto-convection on the Sun [40]. While the principal idea conveyed in (22) is straightforward, the details of the implementation may depend on the form of the equations employed.

For ideal compressible fluids considered in this study, the homogeneity of mass continuity Eq. (14) dictates $\rho^{n+1} \equiv \rho^*$ in (22); whereupon, the time-advanced density is obtained readily by employing a second-order-accurate NFT advection scheme $\mathscr{A}$. For the solvers using either the internal (16) or total energy (17) equations, we construct the first guess $\mathbf{R}^{n+1,0}$ from an auxiliary first-order-accurate solution $\widetilde{\boldsymbol{\Phi}}_i^{n+1}$ of the governing system (20) obtained by reducing (21) to

$$\widetilde{\boldsymbol{\Phi}}_i^{n+1} = \mathscr{D}_i(\boldsymbol{\Phi}^n + \delta t \mathbf{R}^n, \mathbf{V}^{n+1/2}), \tag{24}$$

where $\mathscr{D}$ denotes the generic first-order-accurate upwind scheme – a crude but inexpensive computation. Note that advecting the auxiliary field $\boldsymbol{\Phi}^n + \delta t \mathbf{R}^n$ in (24) is congruent with the first-order Euler-forward trajectory integrals of the Lagrangian counterpart of (20), viz. integrals of the extension of (12) to the vector of dependent variables,

$$\widetilde{\boldsymbol{\Phi}}_i^{n+1} = \widehat{\mathscr{J}}_i \boldsymbol{\Phi}_o + \delta t \widehat{\mathscr{J}}_i \mathbf{R}_o = \widehat{\mathscr{J}}_i (\boldsymbol{\Phi} + \delta t \mathbf{R})_o. \tag{25}$$

Having available first-order estimates of density, energy, and momenta provides the first guess for pressure $\tilde{p}^{n+1}$, and thus for the rhs of the momentum equation. Updating the energy equations – either internal or total – can proceed simultaneously (viz. within the same loop in a computer program) by employing the first guess of their rhs based solely on the auxiliary first-order-accurate solution (24); i.e.,

$$R_{\mathbf{q}}^{n+1,0} = -\nabla \tilde{p}^{n+1} \tag{26}$$

and

$$R_E^{n+1,0} = -\nabla \cdot \left(\frac{\widetilde{\mathbf{q}}^{n+1}}{\tilde{\rho}^{n+1}} \tilde{p}^{n+1} \right) \quad \text{or} \quad R_e^{n+1,0} = -\tilde{p}^{n+1} \nabla \cdot \frac{\widetilde{\mathbf{q}}^{n+1}}{\tilde{\rho}^{n+1}},$$

where tildes refer consistently to first-order predictors, and subscripts at $R^{n+1,0}$ were introduced to denote the conservation law addressed. Alternatively, the momentum and energy equations can be solved in sequence, such that the first guess of an energy equation employs the newly updated momenta; i.e.,

$$R_{\mathbf{q}}^{n+1,0} = -\nabla \tilde{p}^{n+1} \tag{27}$$

but

$$R_E^{n+1,0} = -\nabla \cdot \left(\frac{\mathbf{q}^{n+1,1}}{\rho^{n+1}} \tilde{p}^{n+1} \right) \quad \text{or} \quad R_e^{n+1,0} = -\tilde{p}^{n+1} \nabla \cdot \frac{\mathbf{q}^{n+1,1}}{\rho^{n+1}}.$$

Given $m \geqslant 2$ iterations in (22), both options give essentially the same results, while offering some implementation flexibility. With the auxiliary solution (24), already one successive iteration suffices for the second-order accuracy of the solutions in (22). The subsequent $\mu = 2$ iteration is employed analogously, but with the preceding iterates in lieu of (24). As pointed out earlier in Section 2, its role is to suppress the amplitude errors in representing wave motions [10].

The set of conservation laws using the modified form of the total energy Eq. (18) allows for designing even a simpler algorithm. Because it updates both ρ and E via integrating homogeneous advection Eqs. (14) and (18), respectively, both $\rho^{n+1} \equiv \rho^*$ and $E^{n+1} \equiv E^*$. Consequently, only the momentum-component equations need to be iterated according to (22), to determine $p^{n+1,\mu-1}$ and its gradient from $(\mathbf{q}^{n+1,\mu-1})^2$, ρ^{n+1}, and E^{n+1}. Note that using the linearly-extrapolated modified transport velocity $\widetilde{\mathbf{V}}^{n+1/2}$ for advecting E reminisces the Adams–Bashforth trajectory integrals of the Lagrangian ODE that underlies (17).

The theoretical considerations so far did not address explicitly the conservativity of the approximations discussed. Nonetheless, from the construction of the scalar template (10) and its extension to the vector of dependent variables (21), it is apparent that the resulting abstract framework (22) is in the conservative form (see Section 12.1 in [41]) provided that all components of $\mathbf{R}$ can be written in the conservative form. In such a case, all dependent variables in any region change only due to the flux through the region boundary, even though the effecting flux function may be quite involving and difficult to write in a closed form. Among the considered scalar PDEs, all with $R \equiv 0$, $R_E = \nabla \cdot (\mathbf{V}p)$ and $R_{\mathbf{q}} = -\nabla p = -\nabla \cdot (p\nabla \mathbf{x})$ qualify, because their discrete representations adhere to the finite-volume integral on the rhs of (2). For the PDE sets consisting of (14) and (15), together with either (17), (18) or (19) the resulting algorithm in (22) is conservative both in the numerical and physical sense (Section 3.3 in [42]); but, neither can be assured for the set of (14)–(16). In general, the algorithms enforcing conservation of the total energy receive the most attention, as they encompass theoretically the broadest range of compressible flows. However, for certain flows the alternative formulations may be more adequate. Problems favoring conservation of Θ may include smooth flows at low Mach numbers – where all formulations are mathematically equivalent – or even flows

with discontinuities, when true thermal variations are overwhelmed by truncation errors of numerical schemes. To substantiate the latter, consider that for weak discontinuities, the entropy production proportional to the third power of perturbation pressure (Section 86 in [43]) translates to $\delta\theta/\theta_o = (\gamma^2 - 1)/(12\gamma^3)(\delta p/p_o)^3 \approx 3 \cdot 10^{-2}(\delta p/p_o)^3$ in air. This value is negligibly small in atmospheric flows; see Section 5 for illustration. For similar reasons, the use of special internal energy based schemes [44] is preferred for flows with very high Mach numbers, where the accuracy of pressure evaluation becomes obscured by large kinetic energies.

3.3. Implementation

The general idea of MPDATA methods and the particular template algorithm (10) or (21), are independent of the spatial discretization. To illustrate this flexibility of the approach, we demonstrate results from two distinct implementations using: (i) a structured data for single-block grids; and (ii) an edge-based data for hybrid structured and unstructured meshes.

Our first implementation is an extension to compressible flows of the EUlerian–LAGrangian (EULAG) model for fluids [29], established in simulation of multiscale geophysical flows [45–47,11,48]. Because EULAG uses continuous mappings for Cartesian grid adaptation to either curvilinear boundaries or flow features, the governing PDE (8) evinces additional complexity due to its tensorial formulation [45,49,46]. Consequently, it is technically more convenient to iterate the momentum and the energy equations in sequence, in the spirit of (27). The tensorial formulation of EULAG assumes homeomorphic mappings. This allows for precise representation of smooth time-dependent curvilinear geometries, while offering fast execution of numerical operations and relative simplicity of massive parallelization of the model code. However, for problems with complex geometry and/or multiply-connected domains a single-block mesh and homeomorphic mappings offer limited capabilities, and a more flexible unstructured/hybrid meshing is favoured.

Our second implementation uses the edge-based unstructured mesh code with a dual-mesh finite-volume discretization. This approach circumvents theoretical complexity of tensorial formulation, by integrating the generic physical form of the governing PDE over arbitrarily-shaped cells. Furthermore, it admits flexible adaptivity of the discretization to the problem geometry and/or flow topology, lending itself well to various mesh adaptivity techniques [12,13]. The inherent theoretical simplicity of the edge-based discretization (free of metric coefficients, multitude of velocity forms, and transformed differential operators) allows for a straightforward realization of (22) by updating the momenta and energy in parallel, in the spirit of (26).

4. Benchmark calculations

4.1. Spherical acoustic wave; zero Mach number limit

Statements appear in the literature implying that upwind approximations are inadequate for simulating propagation of acoustic modes. While this may be true for some upwind schemes, one should withhold generalizations as upwinding may take different forms and operate on a variety of auxiliary dependent variables. In particular, MPDATA is constructed using properties of upwinding, yet it is capable of simulating difficult problems of wave dynamics. For substantiation, we elaborate on the paraphrase [14] of the classical problem of a spherical sound wave propagation; Problem 1 in Section 70 of [43]. The problem considers "a sound wave in which the distribution of density, velocity and other flow variables, depends only on the distance from some point." It employs the spherical wave equation for the velocity potential in the zero free stream Mach number limit. Assuming an initial sphere of radius r_o is compressed so that density excess $\rho' = \delta\rho = $ const for $r \leqslant r_o$ and $\rho' \equiv 0$ otherwise, the problem allows the analytic solution (away from the initial disturbance region) in the form of the spherical shell of thickness $2r_o$, located at $r \in [c_o t - r_o, c_o t + r_o]$, where c_o denotes the speed of sound (constant). Within the shell, $\rho' = 0.5(r - c_o t)\delta\rho/r$; whereupon the gas is compressed in the outer portion of the shell $r > c_o t$ and rarefied in the inner portion $r < c_o t$. Fig. 1 shows the analytic and NFT solutions for an arbitrarily specified initial condition and time t. An isothermal hemispherical density excess of $\rho'/\rho_o = 0.082$ with radius $r_o = 0.2$ m, is centered at the bottom of the $6.38 \times 6.38 \times 3.19$ m³ domain. A free stream flow with $c_o = 340.3$ ms^{-1} is assumed to be at rest. The domain is discretized with $319 \times 319 \times 159$ uniform grid intervals $\delta x = \delta y = \delta z = 0.02$ m; whereby, $r_o = 10\delta x$. Numerical integrations of the posed initial value problem are carried with various options of the EULAG model [Eqs. (16), (17) and (19)] using constant temporal increment $\delta t = 10^{-5}$ s. Boundary conditions are periodic in x and y and rigid in z. Notably, the three EULAG options give indistinguishable results. This is not surprising, as pressure and density perturbations are proportional in this flow regime, so the three solutions should only depend on the mass continuity and momentum equations.

In the absence of a significant free stream flow (here $v \approx c_o \rho'/\rho_o$), the first term on the rhs of the equality in (22) reduces, virtually, to its linear kernel; that is, a centered-in-space (and time, as $\mu \nearrow \infty$) approximation for (20). The resulting algorithm is dispersive [10], and the smooth solution in Fig. 1 is achieved by enhancing diffusivity of the first-order-accurate upwind advection with an $\mathcal{O}(\delta x^2)$ residual, in the spirit of the flux-corrected transport (FCT) methods (see Appendix A for a discussion). To further illustrate the properties of MPDATA-based NFT schemes, we alter the classical problem, by introducing a uniform free stream flow with velocity $u_o = c_o/3$. Fig. 2 highlights numerical results with a display of the normalized pressure perturbation p'/p_o after time $t = 720\delta t$, for the isentropic solution using the thermodynamic conservation law (19). The two curves shown in Fig. 3 complement Fig. 2 with the corresponding results using (16) and (17) instead. The selected time of the figures is long – e.g. one order of magnitude longer than in the Sod benchmark [50] – purposely, to emphasize the
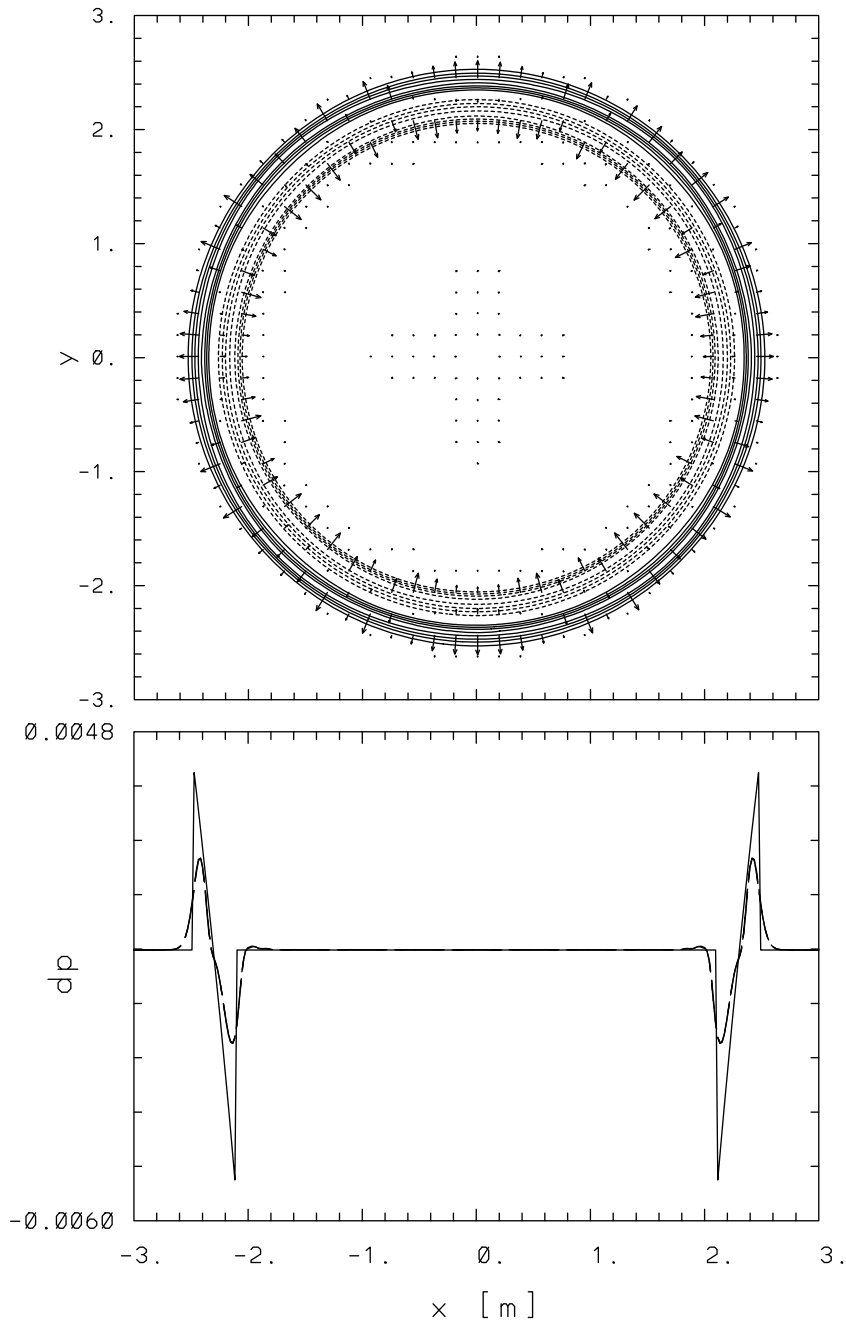
Fig. 1. Spherical sound wave ($M = 0$), normalized pressure perturbation $\delta p = (p - p_o)/p_o$ after $t \gg r_o/c_o$ (r_o is the initial perturbation radius): (top) 3D NFT result in the xy plane at $z = 0$ with superimposed induced flow (max $\|\delta \mathbf{v}\| = 0.6$ ms^{-1}); (bottom) δp at $y = z = 0$ for the analytic solution (solid line) and the three NFT results using Eqs. (16), (17) and (19) (dashed lines).

symmetry, amplitude and phase errors; here $c_o t = 12.25 r_o = 2.45$ m. Except for the value of the free stream flow, this same specification applies to the classical wave propagation problem highlighted in Fig. 1.

Due to the Galilean invariance the modified problem should yield the same solution as the classical problem in the reference frame translating with u_o. Indeed, the result in the top plate of Fig. 2 shows spherical wave propagating radially with c_o, away from the center translating with the free stream flow.[4] The lower plate of Fig. 2 supplements the latter result with the display of normalized pressure perturbation along x at $y = z = 0$. Unlike in the lower plate of Fig. 1 only numerical solutions are

---

[4] We do not show xz cross sections as for all solutions discussed they are indistinguishable from the upper half of the xy images at $z = 0$.

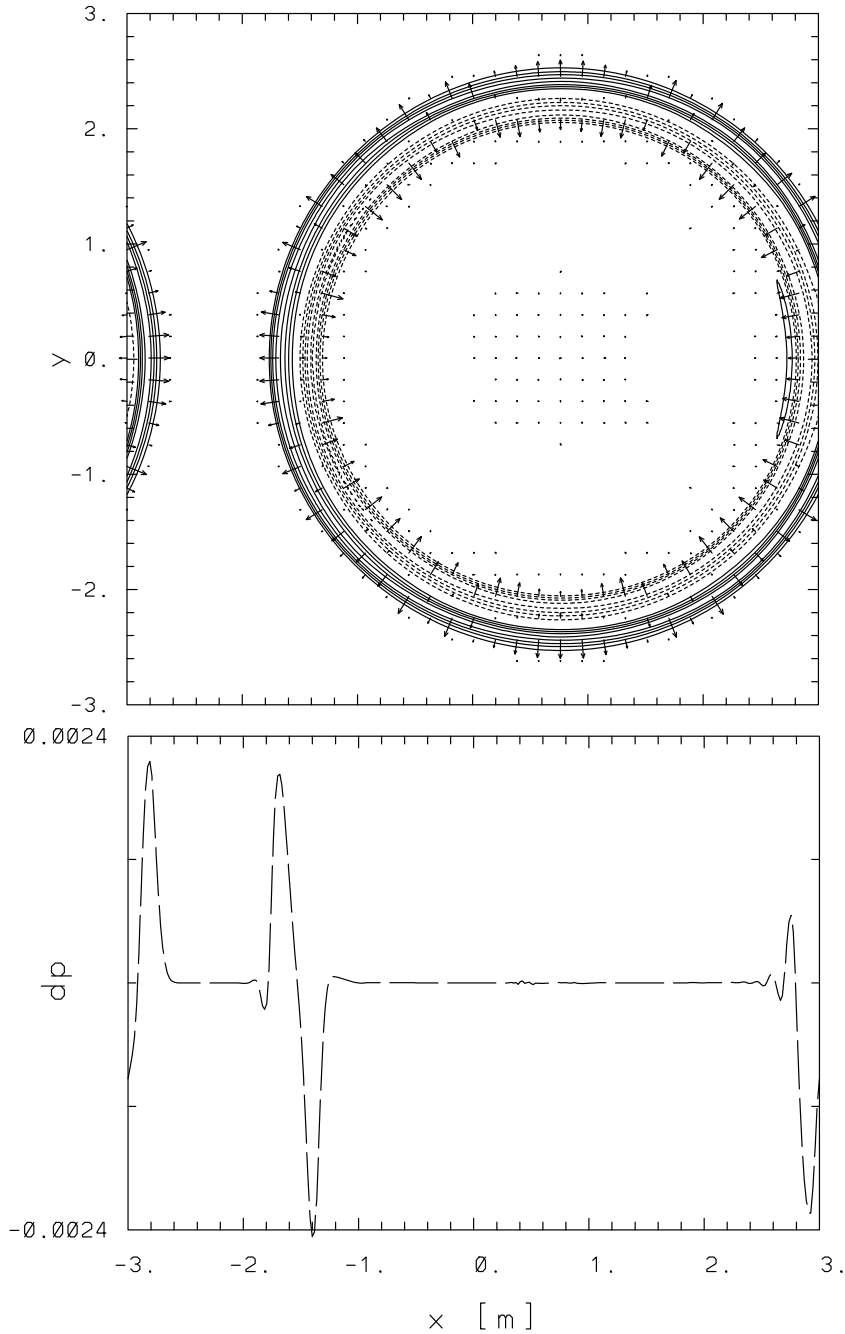**Fig. 2.** Spherical sound wave in $M = 1/3$ free stream flow: (top) isolines of normalized pressure perturbation δp with superimposed perturbation flow $\delta \mathbf{v} = (u - u_o, v)$ vectors (max $\|\delta \mathbf{v}\| = 0.6$ ms^{-1}), in the xy plane at $z = 0$ for the NFT solution using Θ Eq. (19); (bottom) corresponding δp along x at $y = z = 0$.

shown, and the range of the ordinate accordingly reduced. From the two complementary curves in Fig. 3, the one for the calculations using the internal energy Eq. (16) closely matches the isentropic result in Fig. 2. However, the solid curve for the calculation using the total energy Eq. (17) is distinct. The differences between the three solutions are small compared to the difference between all numerical solutions and the theoretical linear estimate, cf. Fig. 1; yet the solution using (17) is clearly more dissipative. Comparing the results in Figs. 2 and 3 with the results in Fig 1, shows a slight symmetry breaking in the modified problem, reflecting the lack of the Gallilean invariance – tantamount to the Courant-number dependence of the truncation error – typical of common second-order advection schemes [20,21]. Here, we used the basic MPDATA scheme with monotonicity-preserving option, and further improvements are possible [4,5]. We shall address some of them as well as the physical significance of the inaccuracies observed, later in the paper.
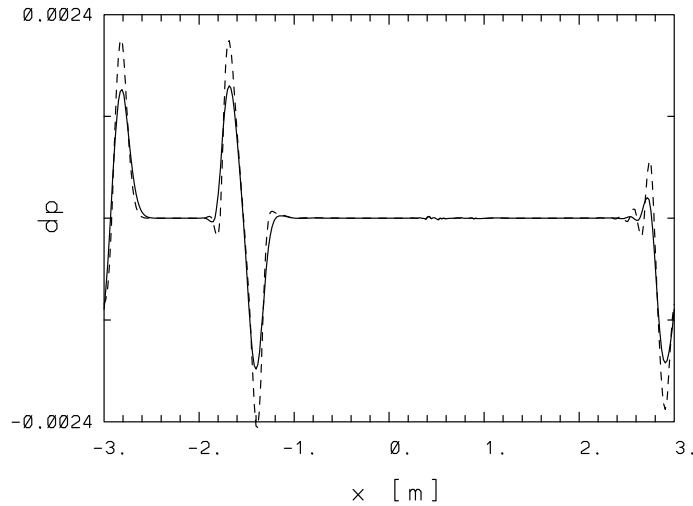
Fig. 3. As in lower plate of Fig. 2 but for the NFT solution using the total (solid line) and internal (dashed line) energy Eqs. (17) and (16), respectively.

4.2. Subsonic flow past a cylinder

The problem represents subsonic steady-state flow past a cylinder, with a free stream initial condition at Mach number $M = 0.38$. The theoretical solution is potential flow, characterized by zero lift and drag; Section 11 in [43]. This test was originally considered in the proceedings from the GAMM workshop held at INRIA Rocquentcourt [51], for the polar 128×33 (4224 points) O-grid. The grid points are angularly equidistributed on 33 concentric circles with consecutive radii starting at $r_1 = 0.5$ and increasing according to

$$r_j = 0.5 \left[1 + \sum_{k=0}^{j-2} \alpha^k \frac{2\pi}{128} \right], \quad j = 2, \ldots, 33, \quad \alpha = 1.1648336;$$

so $r_{33} = 20$ at the outer boundary. Fig. 4 juxtaposes the model grid and 20 Mach number contours in the $[0, 1]$ range for the computations using the modified total-energy Eq. (18). The respective pressure coefficient $- C_p \equiv (p - p_o)/0.5\rho_o \mathbf{v}_o^2$, at $y = 0$ away from the cylinder and along the upper and lower surface at the cylinder $-$ is displayed in Fig. 5. The corresponding solutions for (16), (17) and (19) are not shown, because their departures from the results in Figs. 4 and 5 are insignificant. In all four cases, the single-precision values of the lift and drag coefficients ranged, respectively, from 3×10^{-6} to 1×10^{-6} and from 8×10^{-5} to 6×10^{-5}, attesting to a round-off error accuracy of numerical solutions. Visually, our plots compare well with those shown in [51] (cf. contributions by Dandone et al., Lerat et al., Pandolfi et al., Satofuka et al., and Thomas
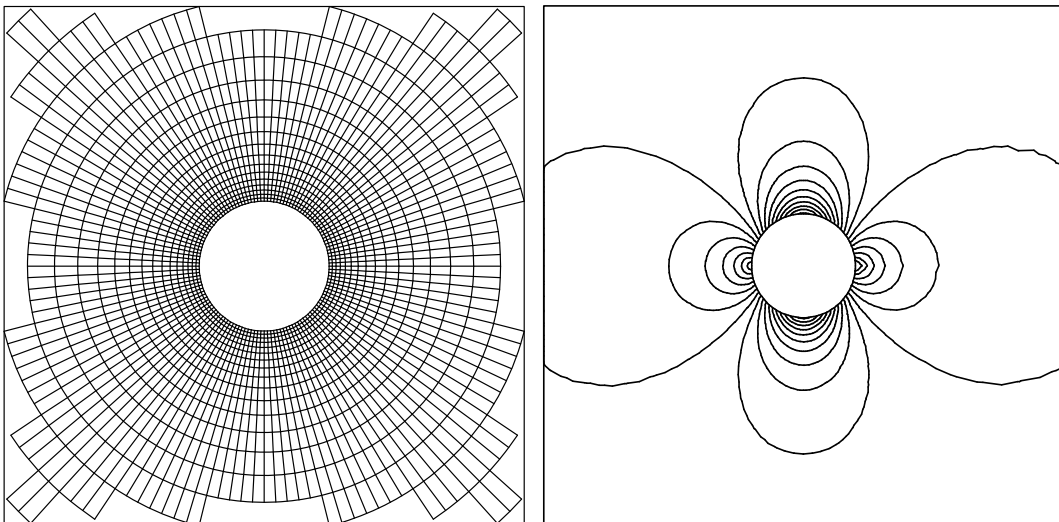

Fig. 4. Flow past a cylinder, $M = 0.38$: (left) computational mesh; (right) Mach number contours, for the modified total-energy Eq. (18).
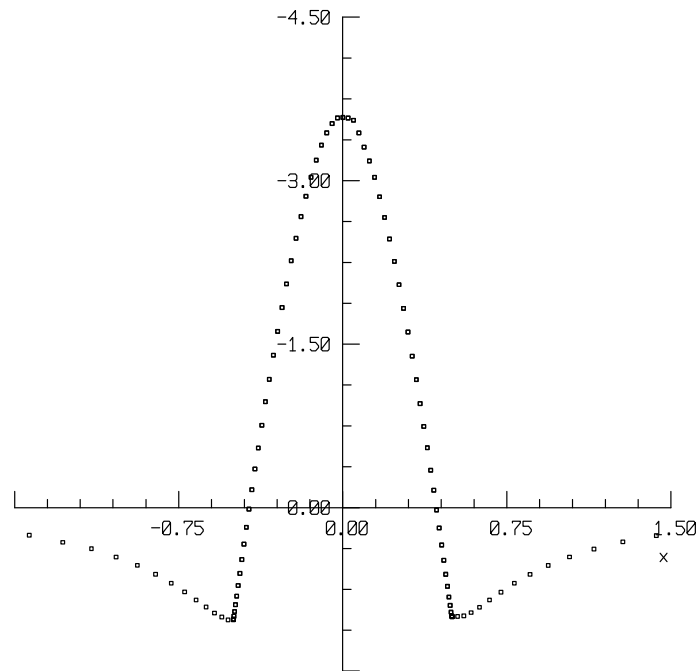
Fig. 5. As in Fig. 4 but for the pressure coefficient.

et al.), especially when taking into account that the test is sensitive to the accurate representation of the surface geometry. Our computations use the edge-based finite-volume discretization, which approximates the shape of cylinder by 128-sided polygon. The use of conformal mapping and curvilinear coordinates, like in some computations included in [51], would increase the accuracy.

Additional results with the edge-based solver were obtained on a triangular, fully unstructured mesh with background spacing purposely similar to that employed in [51] and visually resembling the mesh used in [52]. The mesh was optimised to avoid stretched triangles. It consists of 3773 points, with only 81 boundary points representing the cylinder.

Table 1 compares all our solutions with those published in [52], also obtained on unstructured meshes. It contains the resulting min/max values for local Mach number, pressure p/p_o and entropy deviation $\Sigma = (s - s_o)/s_o$. The upper portion of the table shows the results obtained using selected thermodynamic conservation laws for the MPDATA-based NFT schemes. In the lower portion, we list the corresponding results from Table 3 in [52] generated using MUSCL, the Abgrall's blended and Roe LDA high-resolution schemes.

The MPDATA results are consistent with the other schemes and appear to improve on the MUSCL results in terms of the numerical generation of entropy and the symmetry preservation (not shown). The MPDATA solutions obtained for different

Table 1
Flow past a cylinder

	Mach (Min, Max)	Pressure (Min, Max)	Σ (Min, Max)
Equations; MPDATA			
Structured 128 × 33 O-grid			
Internal energy (16)	0.00000, 0.91	0.64, 1.11	−0.00002, 0.00021
Total energy (17)	0.00000, 0.91	0.62, 1.11	−0.00005, 0.00081
Total energy (18)	0.00000, 0.91	0.63, 1.11	−0.00022, 0.00125
Potential temp. (19)	0.00000, 0.91	0.62, 1.11	0.00000, 0.00001
Unstructured triangular mesh			
Internal energy (16)	0.00001, 0.90	0.64, 1.11	−0.00037, 0.00053
Total energy (17)	0.00000, 0.90	0.63, 1.11	−0.00098, 0.00247
Total energy (18)	0.00000, 0.90	0.63, 1.11	−0.00130, 0.00406
Potential temp. (19)	0.00000, 0.90	0.62, 1.11	−0.00005, 0.00005
Scheme; after [52]			
MUSCL	0.0001, 0.82	0.67, 1.10	−0.0004, 0.048
Abgrall's blended	0.0001, 0.89	0.64, 1.11	0.0, 0.009
LDA	0.0, 0.94	0.62, 1.10	−0.001, 0.010

sets of conservation laws indicate minimal differences between the computations in the min/max Mach number and pressure values. Noteworthy is a low level of entropy, any nonzero value of which is spurious for the isentropic flow considered [52]. The results using the potential temperature equation show that the departure from the free stream value is at the level of round-off error. For the remaining computations the maximum and minimum entropy variations are also very low. However, the presence of negative values of Σ demonstrates that although nonlinearly-stable and robust, the NFT as well as the MUSCL and LDA solutions are not literally oscillation free. The option of MPDATA used here assures merely the monotonicity of advection [12] and employs no additional filtering, neither in the spirit of Section 4.1 nor in the spirit of synchronized limiting for systems of inhomogeneous PDEs [34,35,13].

4.3. Transonic flow

The performance of the outlined NFT algorithms is illustrated next for a steady-state transonic flow over an airfoil – the AGARD test case 04 for the NACA0012 airfoil at Mach number $M = 0.8$ with incidence angle $\alpha = 1.25°$ [53] that requires simultaneous capturing of both strong and weak shocks. The edge-based data structure permits an arbitrary shape of computational cells, therefore we use the same code but employ two distinctly different meshes shown in Fig. 6. The triangular mesh consists of 16101 computational points with 323 points along the airfoil. The quadrilateral C-mesh mesh consists of 30329 computational points with 328 points along the airfoil. Near the airfoil, both meshes use spacing close to that of the structured O-mesh employed in the AGARD test case. In the far field, placed at the distance of 20 chords, boundary conditions are specified from the free stream values or extrapolated from the Riemann invariants, depending on the character of the flow, super- or subsonic, and inflow versus outflow. On the surface of the airfoil a free-slip condition is assumed.
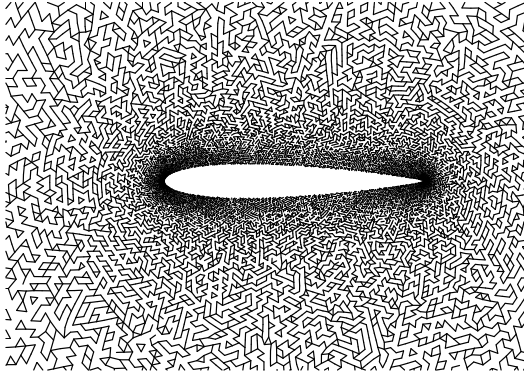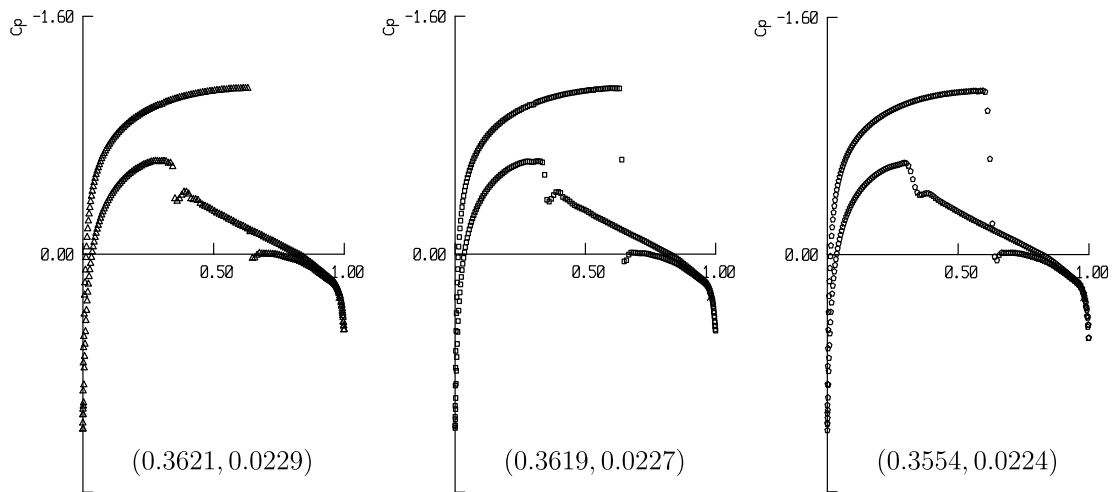
Fig. 8. As in Fig. 7 but for the structured mesh shown in the right panel of Fig. 6.

Figs. 7 and 8 show the standard display of the surface pressure coefficient C_p for the triangular and quadrilateral mesh, respectively, together with the corresponding values of the lift and drag coefficients. The MPDATA results obtained for the standard (17) and modified (18) total-energy thermodynamic conservation laws are compared, showing very close agreement and the sharp (one-point only) shock capturing. Additionally, the MPDATA solutions are compared with the Jameson Runge–Kutta scheme [54]. Results from structured and unstructured meshes show that MPDATA gives a much sharper pressure jump on the weaker lower surface shock (located in the region of higher wall curvature). Results for both meshes also indicate less diffusive capturing of the upper shock in MPDATA.

As in the earlier tests, the presented MPDATA solutions use the monotone option of the scheme in the form detailed in [12]. This option limits the advection velocity used in corrective upwind passes and it is uncoupled for various transported variables. Consequently, without further enhancements, residual oscillations in the vicinity of shocks can appear, as illustrated in Fig. 9. In practice, such oscillations are often suppressed by addition of a pressure-switch-controlled $\mathcal{O}(\delta x^2)$ artificial-viscosity term [54]. In MPDATA schemes these oscillations can be removed more straightforwardly by using a switch-controlled reduction of antidiffusive fluxes in (5); see Appendix in [13]. In effect, at the shock only, the first-order-accurate solution is not fully corrected to the second-order. This enhancement was used to generate solutions in Figs. 7 and 8, but it has been purposely disabled in the calculations presented in the corresponding Fig. 9, to highlight the differences between the NFT algorithms based on the standard and modified forms of the total energy equation. It can be observed that the results obtained using the modified form are less oscillatory, most likely because of the more effective use of the monotonicity constraints in this construction of the MPDATA-based NFT scheme.

A close agreement between the MPDATA results for (17) and (18) forms of total-energy equation was additionally confirmed for the transonic flow over the NACA0012 airfoil at Mach number $M = 0.85$ with incidence angle $\alpha = 1.0°$ [53,51]. The lift coefficient for this problem is known to be very sensitive to the geometrical representation of the airfoil surface and difficult to compute accurately [55]. Despite using a coarse unstructured mesh, Fig. 10, consisting of 3938 computational points with 141 points along the airfoil, the surface pressure coefficients for both forms (17) and (18) show correct, and with one-
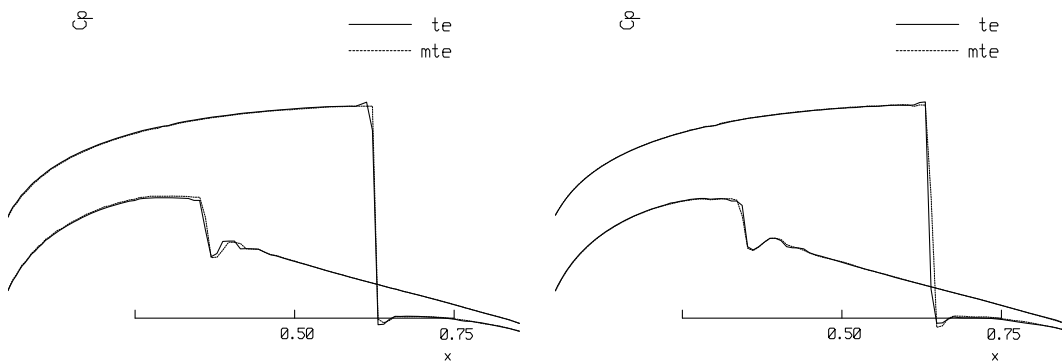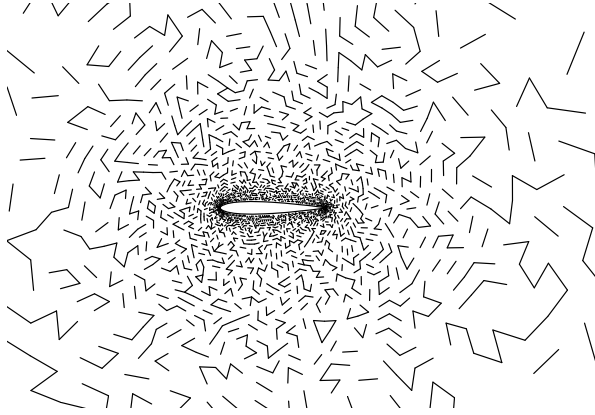

Fig. 9. Surface pressure coefficient for NACA0012 airfoil; $M = 0.8$, $\alpha = 1.25°$. MPDATA results with disabled shock dissipation highlighting differences between the standard and modified total-energy MPDATA based schemes, on triangular (left) and quadrilateral (right) mesh.

point only, capturing of strong shocks on the upper and lower surfaces, Fig. 11. The corresponding pressure contour plot is shown in Fig. 10, for the standard total-energy Eq. (17).

The computed aerodynamic coefficients for both benchmarks are consistent with results published in the literature [51,53]. All calculations used general purpose edge-based MPDATA solvers without any customized treatments for airfoils. An inclusion of the airfoil's surface curvature effects [55], or vortex correction in the far field boundary condition [53] is likely to enhance the accuracy.

4.4. Supersonic flow past a wedge

The results of simulations of supersonic flow over a 15° wedge obtained using two NFT algorithms are compared in Fig. 12 with the theoretical estimation. One algorithm is based on the standard total-energy while the other on the modified total-energy conservation law. The pressure coefficient C_p is used for comparison. For this problem, $C_p = 0.354$ downstream of the shock is estimated from theoretical formulae; pages 754–757, Section 9 in [56]. The corresponding computed values for all wall boundary points placed downstream of the shock are: $C_p \in [0.3347, 0.3561]$ for the standard energy equation (17), and $C_p \in [0.3331, 0.3587]$ for the modified form (18). The minuscule differences between the solutions most likely reflect differences in imposing the monotonicity constraints and effects of additional shock treatment in a form of a pressure-switch-controlled reduction of MPDATA antidiffusion. Both solutions are in a very good agreement with the theoretical estimation. An angle β between the shock and the horizontal can be theoretically evaluated using Eq. (9.22) in [56], i.e.,
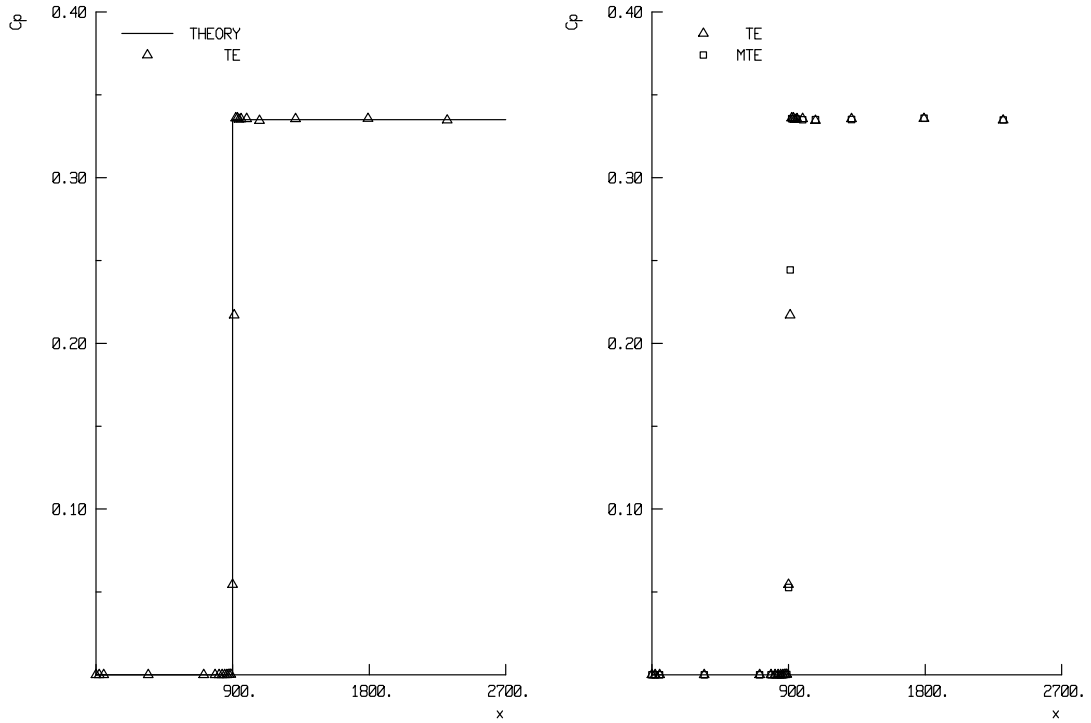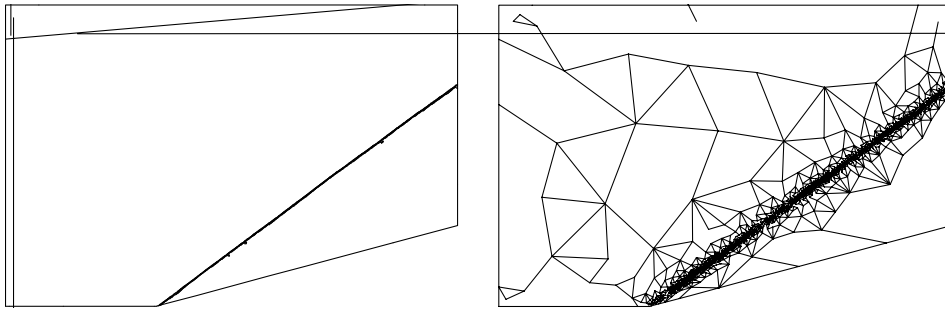
Fig. 12. 15° wedge at $M = 2.5$: (left) the theoretical estimate and MPDATA solution for the total energy equation (TE); (right) comparison of the TE result with corresponding MPDATA solution for the modified total energy equation (MTE).

$$\frac{\tan(\beta - \beta_o)}{\tan \beta} = \frac{2 + (\gamma - 1)M^2 \sin^2 \beta}{(\gamma + 1)M^2 \sin^2 \beta},$$

where β_o is the wedge angle, $\beta_o = 15°$. For $M = 2.5$ and $\gamma = 1.4$, the theoretical value of the angle β is 36.95. The computed values for both algorithms are identical and equal 36.2. Fig. 13 shows pressure contour plots for the standard total energy solution. Pressure contours obtained with the modified total energy equation are practically identical. The computations used the adapted mesh, also shown in Fig. 13, which was obtained using remeshing and the MPDATA-based error indicator [13].

This test case shows that MPDATA effectively resolves supersonic flows. We have successfully repeated the test for higher Mach numbers, up to $M = 15$. Other examples presented in Sections 4.1, 4.2 and 4.3 illustrate the efficacy of the approach for sub- and transonic flows. Note that MPDATA already has a proven record of successful applications for low speed flows [4,31,11]. In the next section we take advantage of the congruity of the template algorithm (10) for the compressible and anelastic flows, and blend the present development with the EULAG's established low-speed anelastic solver to demonstrate the potential of the approach for research of environmental acoustics and extreme events.

5. Extensions to complex media

All examples in Section 4 assume simple homogeneous isotropic media. Such an assumption is sound for small-scale problems, the characteristic scales of which are much smaller than the scales of the medium variability. For gas dynamics of natural atmospheric flows on scales of $\mathcal{O}(10^3)$ m and larger, the variability of ambient temperature, density and wind may need to be accounted for; cf. Chap. 4.6 in [57]. Depending upon the flow regime and focus of interests, this may favor alternate formulations of the thermodynamic conservation laws. Here, we extend earlier considerations to atmospheric mesoscale flows with characteristic length scales $\mathcal{O}(10^4)$ m, and apply the proposed approach to simulation of small and large amplitude acoustic wave phenomena in the framework of the EULAG model. Furthermore, we contrast the solutions realized in variable environments with highly idealized results of Section 4.1, to assess the significance of the disparities between different model formulations and of the solution errors.

The problem posed involves propagation of sound and blast waves in a turbulent strongly stratified orographic flow, and thus blends large- and small-amplitude hyperbolic and dispersive wave dynamics [58]. It is solved in the spirit of so-called secondary application models [59], where an application of interest is driven by an output of a different model. In particular, the anelastic equations [given below in (28)] are employed to generate a fully developed atmospheric flow, which is then used to design initial conditions for simulation of acoustic phenomena with the compressible equations of gas dynamics. The parameters of an undisturbed (ambient) atmosphere are selected purposely to develop a highly inhomogeneous and anisotropic flow. Namely, the ambient stratification is prescribed as $S \equiv d \ln \theta_e(z)/dz = 1.47 \times 10^{-5}$ m^{-1} up to 12 km, but aloft it increases to reflect the isothermal continuation of the ambient potential temperature θ_e. This mimics the thermodynamic structure of the troposphere and lower stratosphere region. At $z = 0$, the surface temperature and potential temperature are both assumed 288.15 K, and the surface density is 1.225 kg/m^3. The ambient wind is $u_e(z) = 10$ m/s up to 12 km, but decreases aloft at the rate $du_e/dz = -0.49 \times 10^{-3}$ s^{-1}. In the troposphere, the imposed wind and stratification support vertically propagating gravity waves with the vertical wavelength $2\pi u_e/N \approx 6.3$ km, where $N = (gS)^{1/2}$ is the buoyancy frequency and g denotes the acceleration of gravity. Furthermore, in the stratosphere, there is a critical level for this wave at $z \approx 14$ km, where wave absorption proceeds via small-scale overturning and turbulence [60]. To excite the wave, a smooth hill is embedded in the ambient flow. The hill is superposed from two cosine profiles $f(x) = h_o 0.5(1 + \cos(\pi x/L))$ with height $h_o = 2.4$ km, and left and right half-width L equal 4.8 and 14.4 km, respectively. The corresponding Froude number $Fr \equiv u_e/Nh_o = 0.35$ indicates violent gravity wave breaking above the mountain with associated windward blocking and severe wind storms in the lee [61].

Fig. 14 shows the intricate initial condition for a 2D (cylindrical) variation on the spherical acoustic wave theme of Section 4.1; cf. Section 71 of [43]. An isothermal circular density excess of $\rho' = 0.1$ kg/m^3 with radius $r_o = 400$ m, is placed at the crest of the hill. The flow shown in Fig. 14 was generated with the anelastic equations of Lipps and Hemler [62], the default option in EULAG. In lieu of (14), (15) and (19) the governing laws for conservation of mass, momentum and thermodynamic properties take the form

$$\nabla \cdot (\mathbf{V}\rho_o) = 0,$$
$$\frac{\partial \rho_o V^I}{\partial t} + \nabla \cdot (\mathbf{V}\rho_o V^I) = -\rho_o \frac{\partial \tilde{p}}{\partial x^I} + g\rho_o \frac{\theta'}{\theta_o} \delta_{I3},$$
$$\frac{\partial \rho_o \theta}{\partial t} + \nabla \cdot (\mathbf{V}\rho_o \theta) = 0.$$
(28)

Here, ρ_o and θ_o denote the density and potential temperature of a horizontally homogeneous static reference state. For discussions of benefits of differentiating between the reference "$_o$" and ambient "$_e$" states, and for examples, see [47,48,29]. The reference state assumes constant stratification $S_o = H^{-1} \ln[\theta_o(H)/(\theta_e(0)]$, with H denoting the depth of the domain; $\theta_o(0) = \theta_e(0)$ and $\rho_o(0) = \rho_e(0)$. Furthermore, $\tilde{p} = p'/\rho_o$, and primes denote perturbations with respect to the ambient state. The anelastic Eqs. (28) are cast in the terrain-following curvilinear framework [49,63] and integrated using the same template algorithm (10), yet with a fully implicit rhs, thus requiring the solution of an elaborate elliptic pressure equation. Integrations are carried for one hour of the simulated time with $\delta t = 0.5$ s, starting from the ambient thermodynamics and initial flow $\mathbf{V}(\mathbf{x}, t = 0) = (u_e, 0) - \nabla \mathcal{X}$ with potential $\mathcal{X}$ determined from elliptic PDE implied by the mass continuity in (28) and the boundary conditions imposed. For recent reviews of relevant numerical details see [47,63]. The $2H \times H = 52 \times 26$ km^2 domain is discretized with 1279×639 grid intervals. The top and lateral boundaries are open, and a free-slip impermeable boundary is assumed at the lower surface of the model.

In general, the anelastic equations prognose potential temperature and velocity but diagnose pressure in the spirit of incompressible models. Consequently, the initial state of the atmosphere for compressible calculations is readily available only for $\mathbf{V}$ and θ. Assuming an initial p' equal to the anelastic value, the actual density ρ is approximated using the linearized ideal gas law

$$\frac{1}{\gamma} \frac{p'}{p_o} = \frac{\theta'}{\theta_o} + \frac{\rho'}{\rho_o}.$$
(29)

Next, the model is restarted as a compressible option of EULAG with the governing Eqs. (14), (19) and (15), cast in the same terrain-following coordinates. The instantaneous state of the atmosphere described above is perturbed with a small density
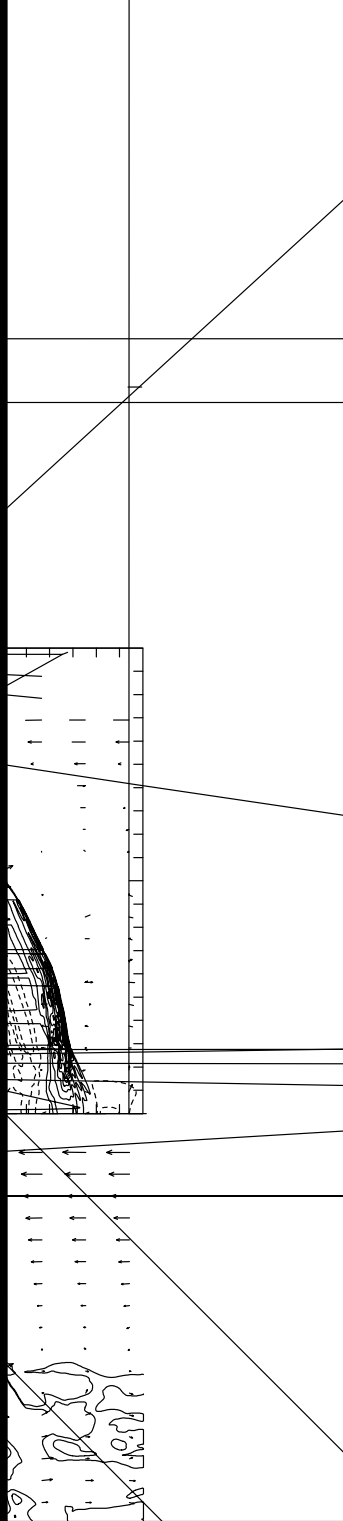
excess discussed earlier and shown in Fig. 14. Furthermore, the momentum Eq. (15) is augmented to include the buoyancy term; that is

$$\frac{\partial q^l}{\partial t} + \nabla \cdot (\mathbf{V}q^l) = -\frac{\partial p'}{\partial x^l} - g\rho'\delta_{l3}. \tag{30}$$

The compressible model is then integrated for over one minute with $\delta t = 0.02$ s, 25 times smaller than for the anelastic calculations. The representative solution is shown in Fig. 15 after $t = 57.6$s.

Inspection of the result in Fig. 15 and its comparison with the initial condition in Fig. 14 shows that despite the severe winds and substantial variability of the environment, the acoustic wave propagates, in essence, as in a frozen atmosphere and retains predominant features of the idealized reference solution for a homogeneous still medium (not shown). The observed departures from the symmetry of the reference solution are all due to interaction with the large scale flow and irregular lower boundary. This has been corroborated by conducting a supplementary study starting with the idealized reference run and gradually complicating it towards the case discussed. Although relatively small, the observed symmetry breakdowns far exceed those due to truncation errors discussed in Section 4.1.

Finally, we augment the previous example, by allowing the small isothermal density excess to be also 1000 K hotter than the environment, thus mimicking a volcano eruption. Fig. 16 shows the result corresponding to the small-amplitude event in Fig. 15. With the larger wave energy, the effects of wave mean-flow interaction become more visible. In particular, the anisotropy of pressure perturbation in the vertical, related to the density decay with height by about the factor of 30 over the model depth, is clearly seen in the stratosphere; cf. Section 106 in [43]. Furthermore, many details of the resulting solution may be argued from the principle of wave-action conservation along the rays, Chap. 4.6 in [57]. However, there are two details important from the perspective of numerical approximation. First, note that the acoustic mode is clearly visible in u and p fields at all depths, but is hardly detectable in contours of θ. This is consistent with the discussion at the end of Section 3.2. Taking a representative stratospheric value of $\delta p/p_o \sim 0.05$ from the central panel of Fig. 16, gives $\delta\theta/\theta_o \sim \mathcal{O}(10^{-6})$ generated at the flow discontinuity. In a stably stratified atmosphere, the equivalent isentrope displacement $\eta \approx (\delta\theta/\theta_o)S_o^{-1} \sim \mathcal{O}(10^{-1})$ m. This is two and four orders of magnitude smaller than the assumed grid interval and the mountain-induced isentropic displacements, respectively. Second, note a small thermal appearing right above the crest of the hill in the upper plate. When solving the problem in terms of the total energy (not shown), the fine features (rolls) of the thermal are dissipated – consistently with the results of Section 4.1 – whereas the gross aspects of the solution appear the same. Together this demonstrates the merits of alternate model formulations.

6. Remarks

We discussed the construction of a new class of the MPDATA solvers. The generality and flexibility of the concept, already proven for incompressible and anelastic flows and Cartesian meshes, is further corroborated with the new schemes customized for compressible flow simulations. Moreover, the numerical examples illustrate the suitability of the approach for unstructured meshes. The experience from the two models – one using Cartesian and one edge-based data type of meshes – shows that the schemes are insensitive to the details of implementation.

Four sets of conservation laws have been integrated using the general NFT framework (10). Their applicability depends on the specific gas dynamics problem. In particular, for subsonic cases, although all four results indicate low implicit diffusion, the simplest potential temperature based algorithm gives the minimum. For transonic and supersonic cases either the standard or the modified (homogeneous) total energy equations can be readily used. Both total-energy models give virtually identical results with narrow shocks. For transonic flows, a one-point oblique shock capturing on structured and unstructured meshes attests to the multidimensionality of the MPDATA solvers. We are not aware of earlier considerations of the total energy conservation equation written in the homogeneous form of the advection equation. Its implementation within the NFT framework results in an especially simple and efficient model. The representation of the total energy equation in an advection form (18) may prove beneficial in development of other types of solvers for gas dynamics.

Our results demonstrate the validity of the approach for a range of compressible flows from zero to supersonic Mach numbers. This extends the utility of MPDATA solvers to a variety of interdisciplinary applications, including the simulation of environmental acoustics and atmospheric responses to localized large-amplitude perturbations. In environmental gas dynamics the effects due to the anisotropy and inhomogeneity of the media (together with uncertainty of the initial and boundary conditions) appear to supersede disparities of various theoretical formulations. Because the preferred formulations of atmospheric fluid equations are still in debate [64], having a suite of schemes operating on various thermodynamic conservation laws is advantageous.

Among several demonstrated merits of the approach, the most distinctive appears to be its universal robustness, evidenced by the ability to provide consistently stable and accurate results throughout the spectrum of flows, irrespectively of the discretization details and types of computational meshes. The close affinity of particular NFT schemes has important implications. First, it facilitates designing of alternative fluid models for multiscale, multiphysics flows. Second, it minimizes uncertainties associated with ad hoc code comparisons, thus enabling unerring analysis of alternate theoretical formulations of complex fluid systems; see [38,48] for examples.

Appendix A. Filtering with MPDATA

For an elementary 1D advection problem

$$\frac{\partial \psi}{\partial t} + \frac{\partial u \psi}{\partial x} = 0 \tag{31}$$

with constant velocity u, the modified equation resulting from the donor cell approximation to (31) can be written as

$$\frac{\partial \psi}{\partial t} + \frac{\partial u \psi}{\partial x} = \frac{\partial}{\partial x}\left(\frac{1}{2}(|u|\delta x - u^2 \delta t)\frac{\partial \psi}{\partial x}\right). \tag{32}$$

In MPDATA, at each time step the action of the error term on the rhs of (32) is compensated by repeating the donor cell step, but using the newly updated ψ and the antidiffusive velocity

$$\widetilde{u} = \frac{1}{2}(|u|\delta x - u^2 \delta t)\frac{1}{|\psi|}\frac{\partial |\psi|}{\partial x}, \tag{33}$$

in lieu of the initial ψ and physical velocity u; for technical exposition see [4,5] and references therein. Clearly, as $|u| \searrow 0$ the dissipative term on the rhs of (32) vanishes, and the implicit viscosity of the upwind scheme becomes insignificant. In applications of (8) with forcing R leading to dispersive oscillations in the numerical representation (10), it may be desirable to enhance diffusivity of the first donor cell step in MPDATA. In the spirit of the FCT methods — cf. appendix in [65] — we add a small explicit Fickian flux $K\partial \psi/\partial x$ in the generic donor cell step, to compensate for it in the subsequent corrective iteration. Such an explicit diffusion augments the modified Eq. (32), resulting in

$$\frac{\partial \psi}{\partial t} + \frac{\partial u \psi}{\partial x} = \frac{\partial}{\partial x}\left(\frac{1}{2}(|u|\delta x + 2K - u^2 \delta t)\frac{\partial \psi}{\partial x}\right). \tag{34}$$

The action of the explicit dissipation can be reverted to $\mathcal{O}(\delta t, \delta x)$ with minimal modifications to standard MPDATA schemes; simply by replacing (33) with

$$\widetilde{u} = \frac{1}{2}(|u|\delta x + 2K - u^2 \delta t)\frac{1}{|\psi|}\frac{\partial |\psi|}{\partial x}, \tag{35}$$

in the subsequent, corrective upwind step.

The outlined procedure is merely a practical guideline on how to adapt a useful element of the FCT technology to the MPDATA framework. Its universal utility, however, still needs to be explored. Similarly as with explicit subgrid-scale turbulence models, selections of K will depend on the problems at hand and details of numerics. In the simulation of the acoustic wave propagation in Section 4.1, we employ $K = \beta\delta x^2/\delta t$, with constant $\beta = 0.02$ — one order of magnitude smaller than the value quoted in [65]. With $\delta t \propto \delta x$, the explicit diffusion enters (34) as an $\mathcal{O}(\delta x)$ correction, whereupon its reversal in the corrective donor cell step leaves an $\mathcal{O}(\delta x^2)$ residual. Formally, this appears to admit second-order convergence along the lines of constant $c_o\delta t/\delta x < 1$ in a low Mach number flow regime.

References

[1] O.C. Zienkiewicz, J. Szmelter, J. Peraire, Compressible and incompressible-flow – an algorithm for all seasons, Comput. Method. Appl. Mech. 78 (1990) 105–121.
[2] C. Gatti-Bono, P. Colella, An anelastic all speed projection method for gravitationally stratified flows, J. Comput. Phys. 216 (2006) 589–615.
[3] R. Klein, N. Botta, L. Hofmann, A. Meister, C.D. Munz, S. Roller, T. Sonar, Asymptotic adaptive methods for multiscale problems in fluid mechanics, J. Eng. Math. 39 (2001) 261–343.
[4] P.K. Smolarkiewicz, L.G. Margolin, MPDATA: A finite-difference solver for geophysical flows, J. Comput. Phys. 140 (1998) 459–480.
[5] P.K. Smolarkiewicz, Multidimensional positive definite advection transport algorithm: an overview, Int. J. Numer. Methods Fluids 50 (2006) 1123–1144.
[6] B. Van Leer, Upwind and high-resolution methods for compressible flow; from donor cell to residual-distribution schemes, Commun. Comput. Phys. 1 (2006) 192–206.
[7] P.K. Smolarkiewicz, A simple positive definite advection scheme with small implicit diffusion, Monthly Weather Rev. 111 (1983) 479–486.
[8] P.K. Smolarkiewicz, A fully multidimensional positive definite advection transport algorithm with small implicit diffusion, J. Comput. Phys. 54 (1984) 325–362.
[9] P.K. Smolarkiewicz, On forward-in-time differencing for fluids, Monthly Weather Rev. 119 (1991) 2505–2510.
[10] P.K. Smolarkiewicz, L.G. Margolin, On forward-in-time differencing for fluids: extension to a curvilinear framework, Monthly Weather Rev. 121 (1993) 1847–1859.
[11] P.K. Smolarkiewicz, L.G. Margolin, Studies in Geophysics, in: F.F. Grinstein, L.G. Margolin, W. Rider (Eds.), Implicit Large Eddy Simulation: Computing Turbulent Fluid Dynamics, Cambridge University Press, 2007, pp. 413–438.
[12] P.K. Smolarkiewicz, J. Szmelter, MPDATA: An edge-based unstructured-grid formulation, J. Comput. Phys. 206 (2005) 624–649.

[13] J. Szmelter, P.K. Smolarkiewicz, MPDATA error estimator for mesh adaptivity, Int. J. Numer. Methods Fluids 50 (2006) 1269–1293.
[14] P.K. Smolarkiewicz, J. Szmelter, An MPDATA based solver for compressible flows, Int. J. Numer. Methods Fluids 56 (2008) 1529–1534.
[15] G. Patnaik, J.P. Boris, T.R. Young, F.F. Grinstein, Large scale urban contaminant transport simulations with MILES, J. Fluid Eng. Trans. ASME 129 (2007) 1524–1532.
[16] S.J. Thomas, J.P. Hacker, P.K. Smolarkiewicz, R.B. Stull, Spectral preconditioners for nonhydrostatic atmospheric models, Monthly Weather Rev. 131 (2003) 2464–2478.
[17] W.J. Rider, The relationship of MPDATA to other high-resolution methods, Int. J. Numer. Methods Fluids 50 (2006) 1145–1158.
[18] P.K. Smolarkiewicz, T.L. Clark, The multidimensional positive definite advection transport algorithm: Further development and applications, J. Comput. Phys. 67 (1986) 396–438.
[19] D.P. Bacon et al, A dynamically adapting weather and dispersion model: the operational environment model with grid adaptivity (OMEGA), Monthly Weather Rev. 128 (2000) 2044–2076.
[20] P.K. Smolarkiewicz, W.W. Grabowski, The multidimensional positive definite advection transport algorithm: nonoscillatory option, J. Comput. Phys. 86 (1990) 355–375.
[21] L.G. Margolin, P.K. Smolarkiewicz, Antidiffusive velocities for multipass donor cell advection, SIAM J. Sci. Comput. 20 (1998) 907–929.
[22] R.F. Warming, B.J. Hyett, The modified equation approach to the stability and accuracy analysis of finite-difference methods, J. Comput. Phys. 14 (1974) 159–179.
[23] P.K. Smolarkiewicz, V. Grubišić, L.G. Margolin, On forward-in-time differencing for fluids: stopping criteria for iterative solutions of anelastic pressure equations, Monthly Weather Rev. 125 (1997) 647–654.
[24] G. Strang, On the construction and comparison of difference schemes, SIAM J. Numer. Anal. 5 (1968) 506–517.
[25] P.K. Smolarkiewicz, J.A. Pudykiewicz, A class of semi-Lagrangian approximations for fluids, J. Atmos. Sci. 49 (1992) 2082–2096.
[26] P.K. Smolarkiewicz, G.A. Grell, A class of monotone interpolation schemes, J. Comput. Phys. 101 (1992) 431–440.
[27] C. Truesdell, The Mechanical Foundations of Elasticity and Fluid Dynamics, Gordon and Breach Science Publishers Inc., New York, 1966.
[28] P.K. Smolarkiewicz, L.G. Margolin, On forward-in-time differencing for fluids: An Eulerian/semi-Lagrangian nonhydrostatic model for stratified flows, Atmos. Ocean 35 (1997) 127–152.
[29] J.M. Prusa, P.K. Smolarkiewicz, A. Wyszogrodzki, EULAG, a computational model for multiscale flows, Comput. Fluids 37 (2008) 1193–1207.
[30] L.G. Margolin, P.K. Smolarkiewicz, Z. Sorbjan, Large-eddy simulations of convective boundary layers using nonoscillatory differencing, Physica D 133 (1999) 390–397.
[31] P.K. Smolarkiewicz, J.M. Prusa, Forward-in-time differencing for fluids: simulation of geophysical turbulence, in: D. Drikakis, B.J. Guertz (Eds.), Turbulent Flow Computation, Kluwer Academic Publishers, Dordrecht, 2002, pp. 279–312.
[32] J.A. Domaradzki, Z. Xiao, P.K. Smolarkiewicz, Effective eddy viscosities in implicit large eddy simulations of turbulent flows, Phys. Fluids 15 (2003) 3890–3893.
[33] L.G. Margolin, W.J. Rider, F.F. Grinstein, Modeling turbulent flow with implicit LES, J. Turbul. 7 (2006) 1–27.
[34] W.W. Grabowski, P.K. Smolarkiewicz, Monotone finite-difference approximations to the advection-condensation problem, Monthly Weather Rev. 118 (1990) 2082–2097.
[35] C. Schär, P.K. Smolarkiewicz, A synchronous and iterative flux-correction formalism for coupled transport equations, J. Comput. Phys. 128 (1996) 101–120.
[36] L.A. Bauer, The relation between potential temperature and entropy, Phys. Rev. (Series I) 26 (1908) 177–183.
[37] K. Maurin, Analysis Part I: Elements, Reidel Publishing Company, Boston, 1976.
[38] P.K. Smolarkiewicz, L.G. Margolin, A.A. Wyszogrodzki, A class of nonhydrostatic global models, J. Atmos. Sci. 58 (2001) 349–364.
[39] C.S. Cotter, P.K. Smolarkiewicz, I.N. Szczyrba, A viscoelastic model for brain injuries, Int. J. Numer. Methods Fluids 40 (2002) 303–311.
[40] P.K. Smolarkiewicz, M. Ghizaru, P. Charbonneau, MHD simulations of the solar convection zone with an atmospheric model, 2007 Workshop on Solution of Partial Differential Equations on the Sphere, 24–27 September, Exeter, UK. <http://www.metoffice.gov.uk/conference/pdes2007/presentations.html>.
[41] R.J. LeVeque, Numerical Methods for Conservation Laws, Birkhäuser Verlag, 1992. 214 p.
[42] E.F. Toro, Riemann Solvers and Numerical Methods for Fluid Dynamics, second ed., Springer, 1999. 624 p.
[43] L.D. Landau, E.M. Lifshitz, Fluid Mechanics, Elsevier, 2004. 539 p.
[44] L.G. Margolin, M. Shaskhov, P.K. Smolarkiewicz, A discrete operator calculus for finite difference approximations, Comput. Method. Appl. Mech. 187 (2000) 365–383.
[45] J.M. Prusa, P.K. Smolarkiewicz, An all-scale anelastic model for geophysical flows: dynamic grid deformation, J. Comput. Phys. 190 (2003) 601–622.
[46] P.K. Smolarkiewicz, J.M. Prusa, Toward mesh adaptivity for geophysical turbulence: continuous mapping approach, Int. J. Numer. Methods Fluids 47 (2005) 789–801.
[47] A. Warn-Varnas, J. Hawkins, P.K. Smolarkiewicz, S.A. Chin-Bing, D. King, Z. Hallock, Solitary wave effects north of Strait of Messina, Ocean Model 18 (2007) 97–121.
[48] P.K. Smolarkiewicz, A. Dörnbrack, Conservative integrals of adiabatic Durran's equations, Int. J. Numer. Methods Fluids 56 (2008) 1513–1519.
[49] N.P. Wedi, P.K. Smolarkiewicz, Extending Gal-Chen & Somerville terrain-following coordinate transformation on time-dependent curvilinear boundaries, J. Comput. Phys. 193 (2004) 1–20.
[50] G.A. Sod, A survey of several finite difference methods for systems of nonlinear hyperbolic conservation laws, J. Comput. Phys. 27 (1978) 1–31.
[51] A. Dervieux, B. Van Leer, J. Periaux, A. Rizzi, Numerical Simulation of Compressible Euler Flows, Notes on Numerical Fluid Mechanics (Vieweg Wiesbaden) 26 (1989).
[52] R. Abgrall, Toward the ultimate conservative scheme: following the quest, J. Comput. Phys. 167 (2001) 227–315.
[53] Test Cases for Inviscid Flow Field Methods, AGARD Advisory Report, 1985, No. 211 AGARD-AR-211.
[54] A. Jameson, W. Schmidt, E. Turkel, Numerical solution of the Euler equations by finite volume methods using Runge–Kutta time-stepping schemes, AIAA 81-1259 Paper.
[55] L. Krivodonova, M. Berger, High-order accurate implementation of solid wall boundary conditions in curved geometries, J. Comput. Phys. 211 (2006) 492–512.
[56] J.D. Anderson, Fundamentals of Aerodynamics, McGraw-Hill Inc., 1991.
[57] J. Lighthill, Waves in Fluids, Cambridge University Press, 1978. 504 p.
[58] G.B. Whitham, Linear and Nonlinear Waves, John Wiley, New York, 1974. 636 p.
[59] R.D. Sharman, Y. Liu, R.S. Sheu, T.T. Warner, D.L. Rife, J.F. Bowers, C.A. Clough, E.E. Ellison, The operational mesogamma-scale analysis and forecast system of the US army test and evaluation command. Part 3. Forecasting with secondary application models, J. Appl. Meteorol. Clim. 47 (2008) 1105–1122.
[60] V. Grubišić, P.K. Smolarkiewicz, The effect of critical levels on 3D orographic flows: Linear regime, J. Atmos. Sci. 54 (1997) 1943–1960.
[61] T.L. Clark, W.R. Peltier, On the evolution and stability of finite-amplitude mountain waves, J. Atmos. Sci. 34 (1977) 1715–1730.
[62] F.B. Lipps, R.S. Hemler, A scale analysis of deep moist convection and some related numerical calculations, J. Atmos. Sci. 39 (1982) 2192–2210.
[63] P.K. Smolarkiewicz, R. Sharman, J. Weil, S.G. Perry, D. Heist, G. Bowker, Building resolving large-eddy simulations and comparison with wind tunnel experiments, J. Comput. Phys. 227 (2007) 633–653.
[64] J. Thuburn, Some conservation issues for the dynamical cores of NWP and climate models, J. Comput. Phys. 227 (2008) 3715–3730.
[65] S.T. Zalesak, A fully multidimensional flux-corrected transport algorithm for fluids, J. Comput. Phys. 31 (1979) 335–362.